A Modular Dual-Polarized Ka-Band Vivaldi Antenna Array

HENRI KÄHKÖNEN[1,2], **JUHA ALA-LAURINAHO**[2], **AND VILLE VIIKARI**[2], **(Senior Member, IEEE)**

[1]Saab Finland Oy, 00100 Helsinki, Finland
[2]Department of Electronics and Nanoengineering, School of Electrical Engineering, Aalto University, 02150 Espoo, Finland

Corresponding author: Henri Kähkönen (henri.kahkonen@aalto.fi)

ABSTRACT A modular dual-polarized Vivaldi antenna array design for 18–30 GHz frequency is presented. The array module consists of the antenna and RF modules. The antenna module comprises 4 × 4 dual-polarized antenna elements with element spacing of λ/2 at 30 GHz. The RF module contains the amplifiers and phase shifters that control all the elements using commercial off-the-shelf (COTS) flip-chip components. The footprint of the RF module is the same as that of the antenna module allowing assembly of antenna arrays of almost any size and shape. Additionally, the interface between the antenna and the RF modules is connectorless, decreasing the number of components required in the assembly and decreasing the overall cost of the system. An array of 4 × 8 dual-polarized antenna elements is constructed from two array modules to prove the seamless operation of the modular design. The prototype uses Anokiwave chips with a frequency range from 26.5 GHz to 29.5 GHz. The measured amplitude and phase of the electric field in front of the antenna aperture is uniform so as to equally feed the elements. Additionally, the demonstrated beam steering up to ±60° in the plane of the larger array dimension matches well with the simulations, proving the feasibility of the design.

INDEX TERMS 5G, antenna array, electronically scanned array, flared-notch antenna, Ka-band, mm-wave, phased array, surface-mounted antenna array, tapered slot, Vivaldi antenna, wideband.

I. INTRODUCTION

Antenna arrays are becoming increasingly important in future mobile networks and sensing applications [1]–[5]. Especially electronically beam-steerable antenna arrays will have the advantage in being able to decrease interference by directing the radiated energy only in the desired direction. Integration of high-performance electronically beam-steerable antennas and the related electrical components becomes increasingly important and at the same time more difficult when moving to higher frequencies, for example, in millimeter-wave (mm-wave) mobile networks. Integrating the amplifiers close to the antenna element decreases losses in the structure, greatly increasing the efficiency and decreasing waste heat. Although, decreasing antenna element size in an antenna array is beneficial to minimize the length of the transmission lines, it also decreases the available area for the

The associate editor coordinating the review of this manuscript and approving it for publication was Giorgio Montisci.

electrical components, such as the amplifiers, phase shifters, and connectors. For example, in an antenna array operating at 30 GHz, the area of one antenna element is approx. 25 mm^2.

There are a few candidates for a wide-band antenna element suitable for phased antenna arrays at mm-wave frequencies, such as the Vivaldi antenna array [6]–[12] and the planar ultrawideband modular antenna (PUMA) array [13]–[17]. PUMA arrays are relatively thin compared to Vivaldi antenna arrays, and they also offer better polarization characteristics when steering in the diagonal plane. However, Vivaldi antennas still have better capability to keep the active reflection coefficient (ARC) below −10 dB when steering beyond ±45° angles, especially in the H-plane. Additionally, a fully metallic Vivaldi antenna can be used as a heat sink for the electrical components when mounted directly on the PCB, and even integrating water-cooling channels within the metallic antenna structure is possible. Conventionally, both PUMA and Vivaldi antenna elements have been constructed so as to have a dedicated connector in each radiating element.

A dual-polarized array, would have two connectors per radiating element. However, fitting these connectors to all the antenna feeds in a dual-polarized antenna array becomes a major issue due to the decreasing size of the antenna elements when the RF-systems move to mm-wave frequencies. In addition to the connector size issue, the cost of the higher frequency connectors also becomes unreasonably high with respect to the manufacturing of the antenna elements.

Other planar antenna structures suitable for mm-wave phased arrays are presented in [18]–[23]. These arrays are mainly manufactured on PCBs and may be manufactured cost-efficiently. These arrays may generally have a narrow bandwidth, narrow beam-steering range, low efficiency due to high dielectric losses, or surface waves in the dielectric. Antenna arrays integrated in the PCB allow the electronics and the antenna elements to be in the same structure and the manufacturing process of these kinds of arrays is well known and reliable [24]–[26]. However, antennas in the PCB require additional layers that increase the cost and complexity of the board. The PCB antennas also prevents the use of additional heat sink components on this side of the board.

In this paper, the objective is to extend the design presented in [27]–[29] and realize the envisioned integration capability of these structures. In the previous works, a similar type of antenna element design is used to confirm the feasibility of the surface-mounted antenna design and the applicability of additive manufacturing to the design to retain good performance up to 40 GHz. This work presents how the antenna array can be directly mounted on top of a PCB without connectors in a modular antenna-array design, placing the beamformer RFICs for Tx/Rx communication behind the antenna array on the same PCB modules and within the same footprint as the antennas for two linear polarizations at 30 GHz. These antenna-array modules enable the array size and shape to be freely chosen, and the cost of the array is decreased by the reduced number of expensive mm-wave RF connectors within the antenna structure. Additive manufacturing is used to manufacture the radiating part of the array, allowing greater freedom in the antenna-array design without increasing the complexity of manufacturing and simultaneously decreasing the cost. The antenna array is designed and optimized using full-wave simulations. Measurements are used to characterize the radiation patterns and the gain of a prototype antenna array to confirm the simulation results.

The article is organized as follows: The antenna element and module designs as well as the measurement board for the proof-of-concept antenna array used to combine the modules together are presented in section II with the simulation results whereas the manufactured structures and the measurement results of the prototype are presented in section III. The paper is concluded in section IV.

II. ANTENNA ARRAY DESIGN
An antenna array prototype is designed integrating previously presented ideas [27]–[29]. The core idea of the antenna array is to be wideband, beam-steerable, modular, and to

theoretically enable the array to be extended to any size and shape. The modularity of the structure includes the integration of the mm-wave front end (RF chips with amplifiers and phase shifters) to provide beam-steering capability to these modules. The antenna and RF modules can then be connected to a single or multiple analog or digital receivers through power-division networks, and the logic controlling the antenna element weights.

The prototype is designed to be a dual-polarized 4×4 Vivaldi antenna array module that can be connected to a measurement board behind the module. The measurement board can be configured with up to four modules forming an array of 8×8 antenna elements or 2×2 antenna modules. Each array module includes a metallic, surface-mounted antenna module and an RF module. The RF modules act as the interface of the antenna modules and includes Anokiwave AWMF-0162 chips with amplifiers and phase shifters. Whereas the designed antenna module is wideband having an operational bandwidth from 18 to 30 GHz, the ICs are designed for the n257 band (26.5 to 29.5 GHz). The modular design allows the AWMF-0162 chips to be replaced with corresponding chips for n258 band (24.25–27.5 GHz). The array modules are connected to a power-division network on a measurement board directly behind these modules. The RF module signals are combined in the feed network on that board such that there is one external port for each of the polarizations. The measurement board is also used to regulate the input voltage to the ICs and combines the digital control lines.

A. ANTENNA MODULE
The radiating part of the antenna array sets the restrictions for the size of the rest of the components due to the element spacing requirement. The antenna element spacing should be close to half a wavelength with respect to the upper frequency limit of the operational band to prevent the rise of grating lobes within the field of view of the array. In this case, half wavelength at 30 GHz implies an element spacing of 5 mm.

The Vivaldi antenna element used in the antenna module is designed for a frequency range between 18 and 30 GHz and is shown in Fig. 1. The most important dimensions are presented in Table 1. The antenna element is based on a dual-polarized Vivaldi antenna design that can be surface-mounted on a PCB. The antenna element is a single piece of metal and can be manufactured using additive manufacturing or electric discharge machining. It is based on the design presented in [27]–[29] with the dimensions scaled and optimized for the frequency range up to 30 GHz. One antenna element is dual polarized, and the elements can be used to construct arrays of various sizes. The size of one element is $5 \times 5 \times 18.5$ mm^3 ($x \times y \times z$).

The simulations have been performed using CST Studio Suite. The simulation results of the antenna element in a unit-cell show that the antenna is matched well in the designed frequency band in the steering range up to $\pm 60°$. Fig. 2 shows the active reflection coefficient (ARC) of the antenna element
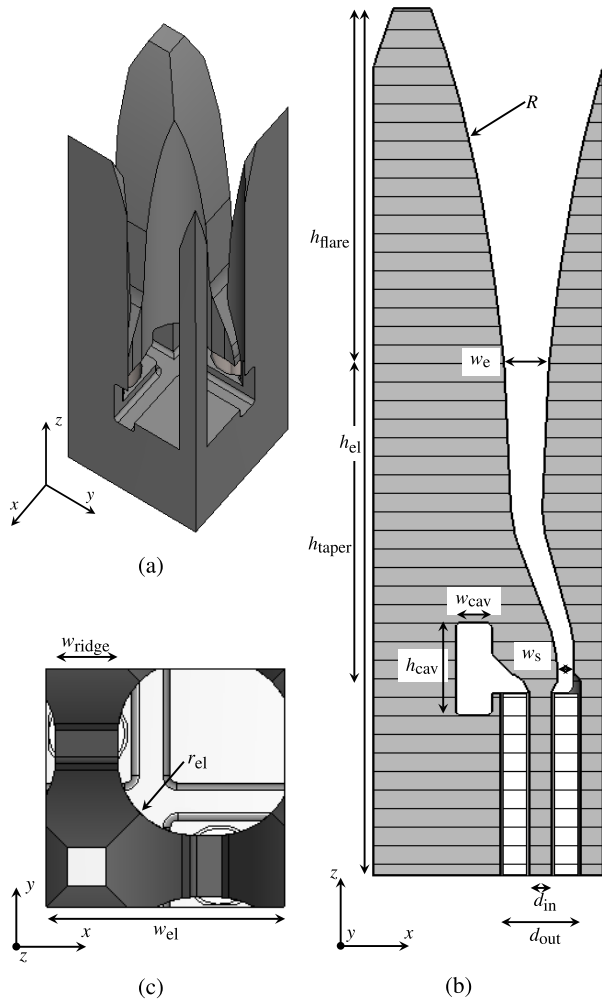
FIGURE 1. (a) 3-D view of the simulated unit-cell antenna element structure, (b) the side view of a section of the antenna element, and (c) the top view of the antenna element.

TABLE 1. Dimensions of the simulated unit-cell structure.

d_{in}	coaxial inner diameter	0.5 mm
d_{out}	coaxial outer diameter	1.8 mm
h_{el}	total height of the element	18.5 mm
h_{flare}	height of the exponential taper	7.8 mm
h_{taper}	height of the linear taper	7.2 mm
h_{cav}	height of the cavity	2.05 mm
R	rate of the exponential taper	0.17
r_{el}	radius in the cutout between the ridges	1.6 mm
w_{cav}	width of the cavity	0.8 mm
w_e	width of the slot after linear taper	1 mm
w_{el}	element spacing	5 mm
w_{ridge}	width of the ridge	1.3 mm
w_s	width of the slot	0.33 mm

between 18 and 30 GHz in the broadside direction, in the ±60° beam steering in the elementary E- and H-planes, and in both diagonal planes. The presented beam steering results in the highest possible ARC within the beam-steering range of the specific antenna element and thus gives a good overall perception of its operation. The ARC is better than −10 dB everywhere else except in the H-plane with ± 60° steering

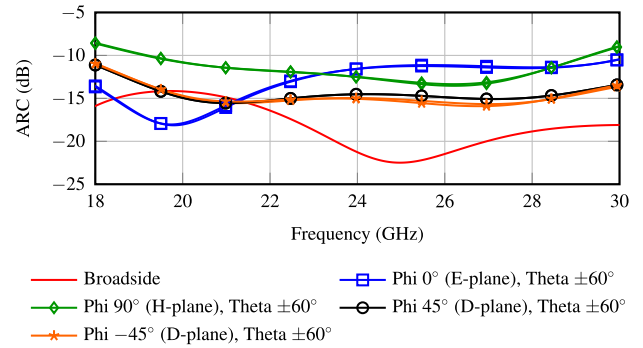**FIGURE 2.** Simulated ARC of the antenna element in the broadside direction, and in the ±60° beam-steering directions in the E-, H-, and D-planes.

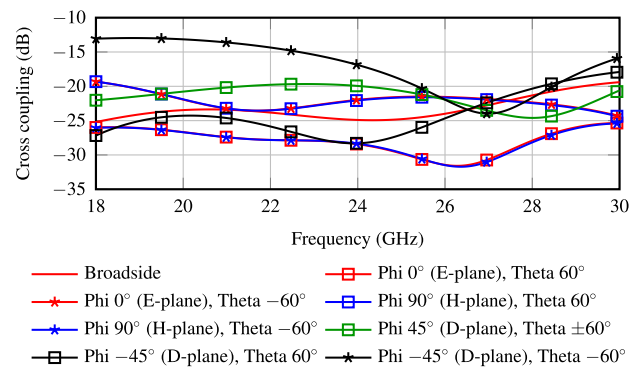**FIGURE 3.** Simulated coupling between the ports of different polarization of the antenna element in the broadside direction, and in the ±60° beam-steering directions in the E-, H-, and D-planes.

below 19.5 GHz and above 29 GHz. Fig. 3 shows the coupling between the ports of the vertical and horizontal polarization. Similarly to the ARC, the cross coupling is also dependent on the beam steering. The behavior of the ARC is approximately symmetric in any given plane but the cross coupling is not. The coupling is generally below −20 dB, but in the $\phi = -45°$ plane (D-plane) it rises above −15 dB below 22.5 GHz when steered to −60°.

Fig. 4 shows the embedded element patterns at 18, 26, and 30 GHz. In the elementary planes, the co-polarized element patterns are close to a cosine function, and the scan loss is approximately −3 dB at ± 60°. The cross-polarization level is generally below −20 dB. In the diagonal planes, the co-polarized pattens are not as wide as on the elementary planes, and the level of the cross polarization increases.

In this demonstration, the elements are arranged in a 4×4 array module. The base of the module is $20 \times 20 \text{ mm}^2$ in size, and the antenna modules can be arranged to form a larger continuous array.

B. RF MODULE
The RF module, containing the integrated amplifiers and phase shifter chips, is designed to interface directly with

FIGURE 5. RF-signal schematic of the RF module. The circles represent RF connectors, and the signal follows the path from the connectors to the ICs from where the signals are guided to the antenna elements.
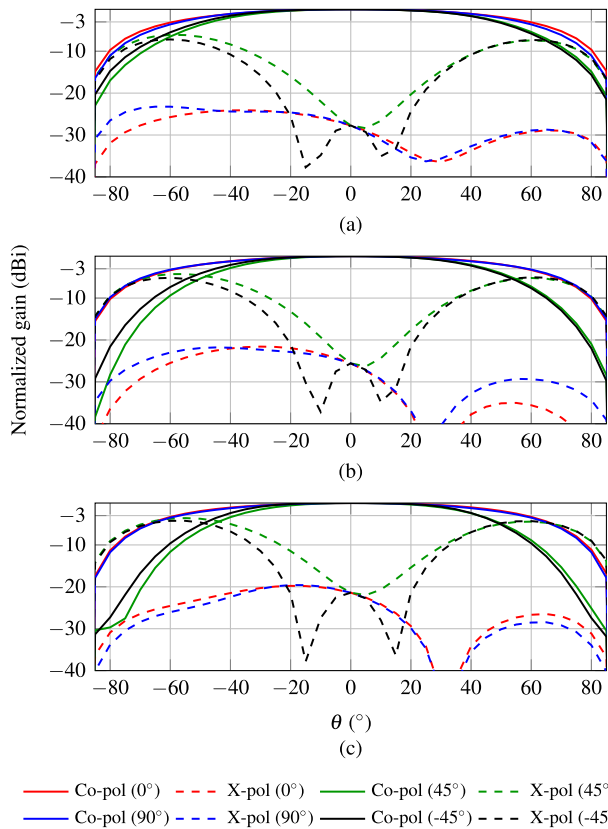

FIGURE 4. Simulated embedded element patterns of the antenna array in a unit-cell simulation at (a) 18 GHz, (b) 26 GHz, and (c) 30 GHz, in the E-, H-, and D-planes.

FIGURE 6. (a) Top view of the PCB which is in contact with the antenna module, and (b) the bottom side of the PCB where the RF chips and the connectors are mounted. Red squares illustrate the chip placement and the numbers indicate the port numbers used in the simulations.

the surface-mounted antenna module without any connectors so that the chips are close to the antenna elements. The connectorless design significantly reduces the cost of the array since expensive RF connectors are not used. The antenna may be attached to the RF module either with screws, with solder, or with a thin film of conductive glue. The RF module design in based around RFICs with amplifiers and phase shifters capable of both TX and RX applications. The Anokiwave AWMF-0162 chips are commercial off-the-shelf (COTS) components with a common port connected to four antenna ports, where the phase and the amplitude of each antenna port can be controlled separately. The operation frequency of these chips is 26.5–29.5 GHz (n257 band).

The transition from each of the antenna elements to the RFICs is designed to be as short as possible to minimize losses and the footprint of the module. The size of the RF module is $20 \times 20\,\text{mm}^2$, the same as that of the antenna module. There are eight Anokiwave AWMF-0162 chips on the module with a total of 32 antenna ports, 16 for each polarization. The ICs are divided so that four are dedicated to the vertical and another four to the horizontal polarization. The common ports of the ICs are connected to four SMPS connectors from which each of the polarizations have two connectors. Fig. 5 shows a schematic of the RF-signal paths
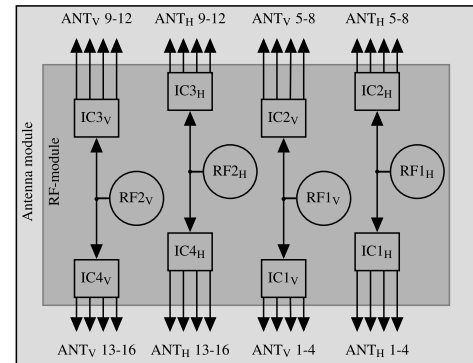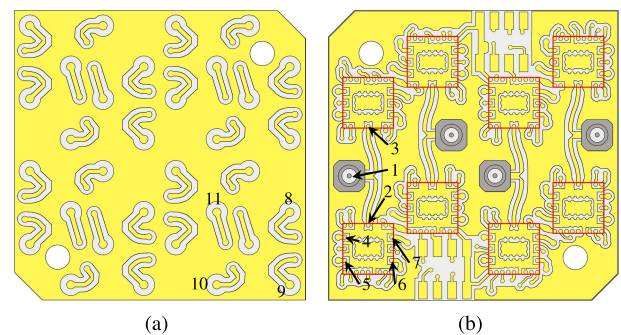
in the RF module. Fig. 6 shows illustration of the top and bottom layers of the RF module where the RF traces are, and the port numbering used in the simulations. Fig. 7 shows more detailed view of the RF traces and the PCB layers and Table 2 shows the indicated dimensions. The PCB is an eight-layer design using 118-μm substrates between the layers. The RF layers on the top and bottom are connected through the board with a plated through hole while other vias are microvias. The inner layers are used for the cavities behind the connector and antenna transitions, and the control and power lines for the chips. The signal enters the RF module from a SMPS connector and the following T-junction power divider splits the signal between two ICs. The IC divides the signal further to four antenna ports. The antenna ports are connected to a short microstrip line that is routed from the bottom layer to the top layer, where another short microstrip line functions as a transition to the coaxial antenna feed.

The ICs are controlled with SPI. On the module, they are arranged in two chains of four chips, as shown in Fig. 8. The control data is passed through the chain of four chips when the chip's select pin is enabled and the telemetry data from the chip is simultaneously pushed back to the controller. In addition to the pins required for the SPI control signals, there are, in all four additional control lines to enable the
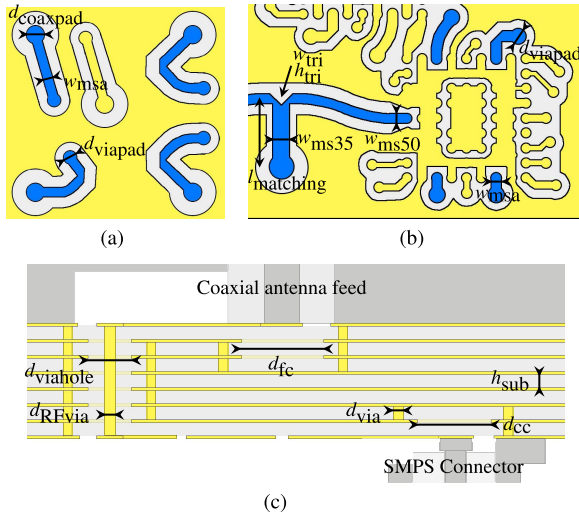
FIGURE 7. (a) a close-up of the antenna feed lines on the top side of the PCB and (b) on the bottom side of the PCB with RF lines for one polarization indicated with blue. (c) illustration the PCB stack-up with the most important features.

TABLE 2. Dimensions of the RF lines in the RF module.

|		
$d_{coaxpad}$	antenna feed pad diameter	0.71 mm
d_{viapad}	RF via pad diameter	0.45 mm
d_{via}	diameter of the laser vias	0.15 mm
d_{RFvia}	diameter of the drilled RF via, nominal (drill)	0.15 (0.2) mm
$d_{viahole}$	diameter of the hole in the ground plane around the via	0.7 mm
d_{fc}	diameter of the cavity under the coaxial feed line	1.3 mm
d_{cc}	connector cavity diameter	1.1 mm
h_{sub}	substrate thickness	118 μm
h_{tri}	height of the triagular cutout	0.3 mm
$l_{matching}$	length of the 35-Ω matching line	1.82 mm
w_{msa}	antenna-feed line width	0.3 mm
w_{ms35}	width of the 35-Ω line	0.35 mm
w_{ms50}	width of the 50-Ω line	0.26 mm
w_{tri}	width of the triangular cutout	0.6 mm
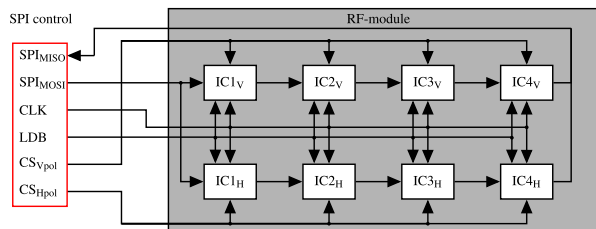
FIGURE 8. Schematic of the SPI logic lines used to control the RFICs. Multiple modules can be arranged parallel to each other on the SPI data, clock, and latch lines.

transmit or receive mode of the chips separately for each polarization.

The module is divided into four identical RF branches. Each of these include the trace from the SMPS connector to the two chips, and each chip is connected to the antenna elements with identical traces. Thus, the simulations included here only present the results for one of these sections. The results for the remaining sections would be
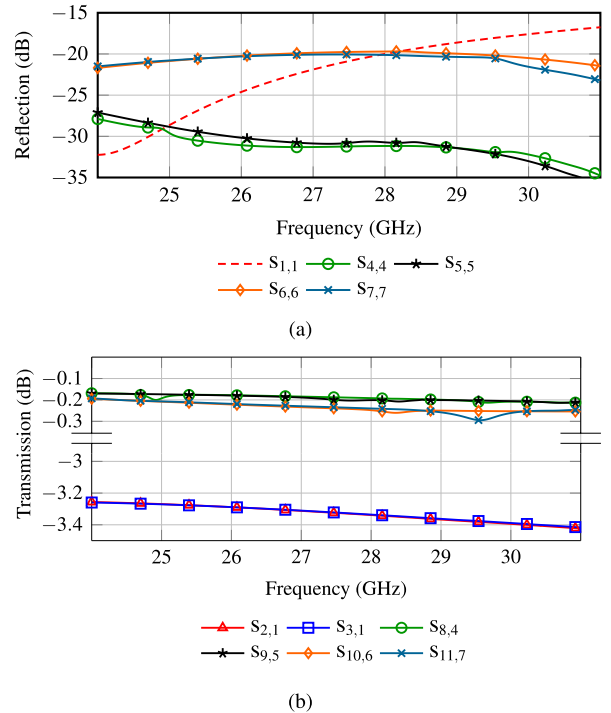

FIGURE 9. Simulated (a) reflection and (b) transmission coefficients of the RF module PCB.

identical to the presented ones. The simulated reflection and transmission coefficients of one RF branches are shown in Fig. 9. The reflection coefficient $s_{1,1}$ is the value simulated from the SMPS connector and includes the power divider and the common 50-Ω ports on two ICs. The reflection coefficient from the connector to the ICs is below −20 dB up to 28 GHz and below −17.5 dB up to 30 GHz. The transmitted power to the ICs is described with the transmission coefficients $s_{2,1}$ and $s_{3,1}$. The transmission coefficients are between −3.2 dB and −3.4 dB. The reflection coefficients of ports 4 and 5 are close to −30 dB in the shown range between 24 and 31 GHz whereas the transmission coefficients from these ports to the corresponding antenna coaxial lines is approximately −0.2 dB. The other two antenna feed lines from the chip to the ports 6 and 7, have the reflection coefficients of approximately −20 dB, and the transmission coefficients of −0.25 dB.

C. MEASUREMENT BOARD

The RF modules can be used to virtually create an array of any size and shape within the limitations of the module geometry. In this prototype, a feed network is designed to accommodate a measurement of a maximum of four dual-polarized modules in an 8 × 8 element configuration. The configuration requires a feed network for four RF modules in a 2 × 2 module configuration resulting in a total of 16 RF inputs, eight for each polarization. This is realized with two RF connectors at the edge of the PCB, one for each polarization, being connected to the RF modules with two trees of Wilkinson power
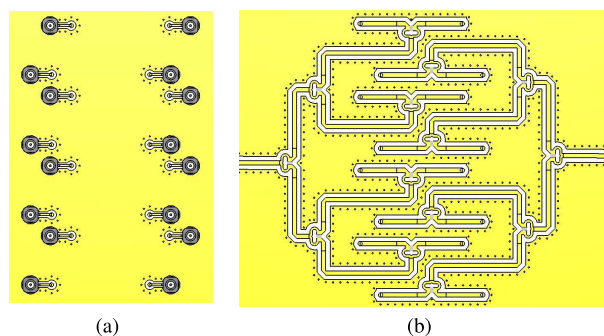
FIGURE 10. Illustration of the simulation model of the power division on the board: (a) the top side of the measurement board showing the SMPS connectors with short microstrip transitions, and (b) the bottom side of the board showing the feed network with the Wilkinson power dividers.

dividers resulting in two separate one-to-eight power division networks, as shown in Fig. 10. The measurement board uses the same SMPS connecters as the RF module, and the RF modules are connected to the measurement board with SMPS bullets. The transitions where the signal passes through the measurement board and the transition from the microstrip line to the SMPS connectors use identical structures as in the RF module. The logic lines, including the SPI clock, SPI data lines, SPI latch, and chip select lines, which route the control signals to the ICs, are also combined on this PCB. In addition to the SPI logic lines, there are also enable signal lines for transmit and receive modes for both polarizations: Tx_V, Tx_H, Rx_V, and Rx_H. These control the state of the chips and are connected to the chips depending on their polarization.

Additionally, the measurement board is used to handle the voltage control of the modules. The board includes linear voltage regulators on one side of the PCB to ensure that the proper voltage level is applied to the RF modules. In this case the voltage is regulated to 1.8 V, the operating voltage of the RF chip amplifiers and the logic. The PCB is designed to be able to handle an input voltage range of 2.5 V to 3.3 V and up to 48 A current which is sufficient to operate four modules and both polarizations in all the antennas simultaneously. The size of the measurement board is $80 \times 80\,\text{mm}^2$

Fig. 11 shows the simulated reflection and transmission coefficients of the feeding network of one polarization. $s_{1,1}$ is the reflection coefficient of the edge-launch connector, and the eight other ports represent the antenna module ports with SMPS connectors. Similarly, the transmission coefficients illustrate the coupled power from the edge-launch connector to the module connectors. The $s_{1,1}$ is less than $-15\,\text{dB}$ in the frequency range from 24 GHz to 31 GHz whereas the reflection coefficient of the other ports is less than $-20\,\text{dB}$. The transmission coefficient from the board-edge port to the SMPS connectors is $-12.5 - -11.5\,\text{dB}$.

III. MANUFACTURED STRUCTURE AND MEASUREMENT RESULTS
The goal of the measurements is to confirm the operation of the complete structure combined from separate modules.
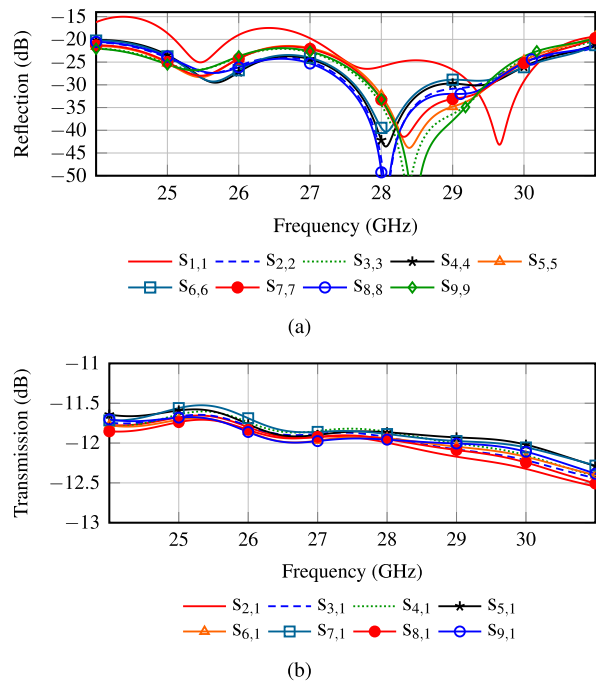

FIGURE 11. (a) Simulated reflection and (b) transmission coefficients of the measurement board.

Simulations were used to design the following separate structures: the transition from the edge-launch connector to the common port of the RF chip and the transition from the antenna port of the RF chip to the antenna feed. Also, simulations of the operation of the antenna in unit cell and in full array configuration were performed.

A. MANUFACTURED STRUCTURES
The manufactured structures include the additively manufactured antenna module shown in Fig. 12. The antenna modules were manufactured from 316L stainless steel with binder jetting. Binder jetting is an additive manufacturing technique that can be used for both plastics and metals but, the methods are different for the two materials. For metallic structures, the metal powder is first bound using a binding agent to form a scaled-up shape of the part. Then the formed part is heated in a high-temperature oven to first dissipate the binding agent and then to sinter the metal particles together.

316L stainless steel was selected as the material to manufacture the antennas based on experience in [29]. Additionally, a trial run with the same manufacturing method was made using copper powder. However, the copper structures failed during sintering mainly around the coaxial feed pins due to the softness of copper unlike the stainless steel.

The antenna module size is $20 \times 20 \times 18.5\,\text{mm}^3$ ($x \times y \times z$). The coaxial antenna feeds can be seen at the bottom of the antenna module. Cutouts for the microstrip feeding lines are seen in Fig. 12 (c). Additionally, the coaxial feeds are filled with PTFE inserts to achieve an impedance of 50 Ω. The dimensions of the manufactured parts are in line
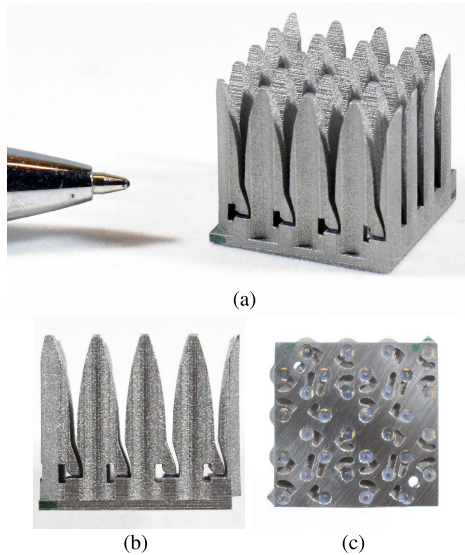
FIGURE 12. (a) One manufactured 4 × 4 antenna module with the tip of a ball-point pen alongside as a scale, (b) a side view of the antenna module, and (c) the base of the antenna module.
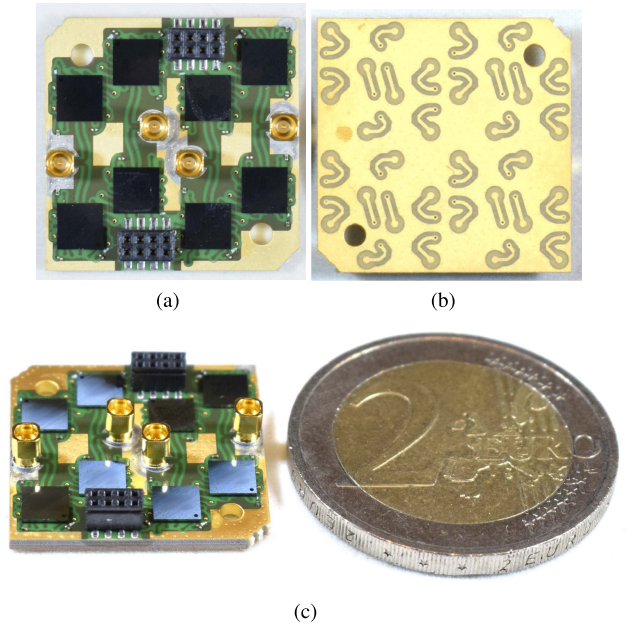

FIGURE 13. Images of one RF module: (a) the bottom of the module where the RF chips and connectors are placed, (b) the top of the RF module where the antenna interface is visible, and (c) the RF module with a two-euro coin as a scale.

with the design parameters. The bottom of the antenna was machined flat after the printing process to achieve better contact between the antenna module and the RF-module PCB. The antenna and the RF modules are attached with screws.

Fig. 13 shows the bottom of one manufactured RF module where the surface-mounted components are, the top where the antenna feed lines are, and a two-euro coin as a scale to illustrate the small size of the module. In addition to the RF chips, there are four SMPS connectors for the RF signals, two 1-mm eight-position socket connectors, and 01005 capacitors required by the ICs.

Fig. 14 shows the manufactured measurement board capable of supporting a maximum of four antenna and RF modules. The top side of the PCB includes connectors corresponding to the RF-module connectors and linear voltage regulators to ensure that the proper voltage is fed to the RF modules. The feeding networks for the two polarizations are visible on the bottom of the PCB. The feed network is realized with Wilkinson power dividers. Edge-launch connectors are used to connect the PCB to the measurement device.

During preparation of the antenna array measurements, the RF modules and the operation of the chips were tested. In some modules, one or more of the chips had issues with the SPI data line. The control data either did not pass through the chip or the passed data was distorted in the SPI chain. The issue rendered some RF-module PCBs uncontrollable, and the measurements were hence performed with two operational modules in a dual-polarized 4 × 8 antenna array configuration.

B. MEASUREMENTS

The measurements were performed with a 4 × 8 antenna array due to the previously mentioned issues with the SPI

data lines used to control the ICs. The measurements were performed using a near-field scanner where an open-ended waveguide (OEWG) probe was moved in front of the antenna-under-test, and the amplitude and phase of the electric field was measured at multiple points with a spacing of $\leq \lambda/2$. Fig. 13 shows the assembly of the prototype with two antenna and RF modules and the measurement setup. The antenna array is oriented such that there are eight antenna elements along the vertical axis and four along the horizontal. A far-field transform is performed on the measured data to acquire the far-field patterns.

Fig. 16 presents the measured co-polarized electric field in front of the antenna array aperture at 28 GHz when the array is excited with a uniform amplitude and phase. Both the amplitude and the phase of the E-field for both vertical and horizontal polarizations are smooth across the aperture. Even though the antenna aperture is assembled from two separate modules with a very small gap between the radiating elements, there is no observable effect, and the measured results look similar to those of a continuous antenna array structure.

Fig. 17 shows the normalized far-field patterns in the broadside direction on the V- and H-planes at 26.5 and 29.5 GHz. In these planes, the patterns are close to the simulated results, but there is some variation in the side-lobe levels. The main lobes of both polarizations are almost identical further indicating there are no issues with the antenna elements or the feeding structure. Fig. 18 shows measured total gain of the system, simulated directivity and realized gain of the antenna, and two estimations of the measured realized gain of the antenna in the broadside direction.
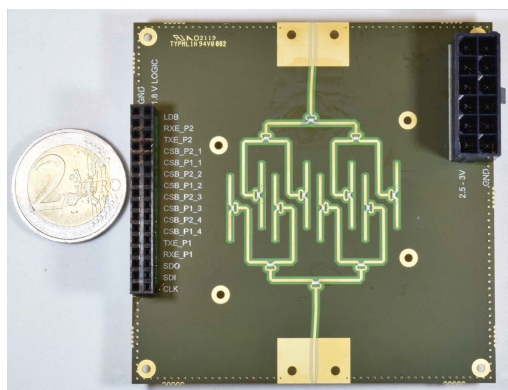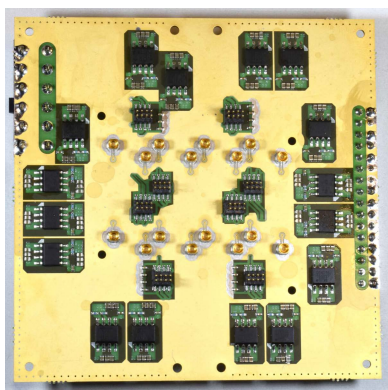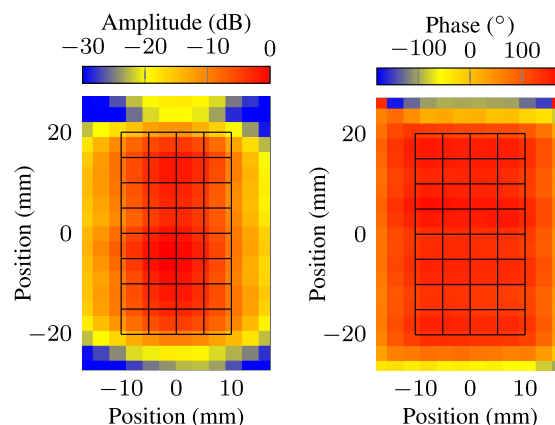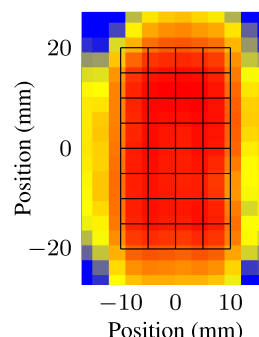
FIGURE 14. The measurement PCB for connecting up to four antenna array modules: (a) the bottom of the PCB with the power division network and (b) the top of the PCB with the connections to the antenna array modules and the linear voltage regulators.
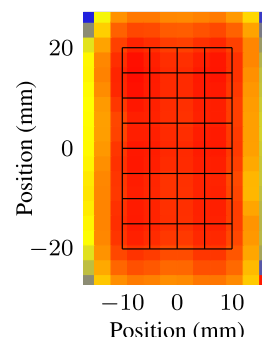

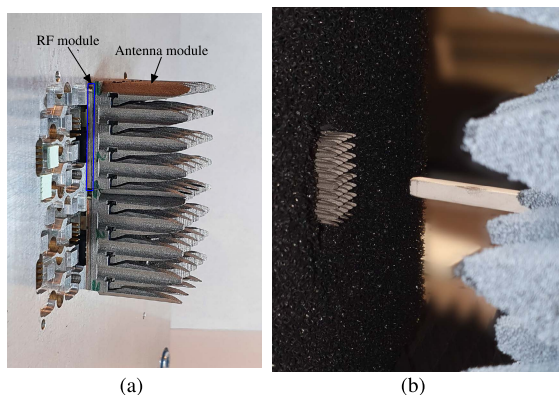**FIGURE 15.** (a) Photo of the assembly with two antenna and RF modules on an aluminum mounting plate and (b) the measurement setup where the 4 × 8 antenna array is positioned in front of the open-ended waveguide probe.

The total gain is 36.6–39.5 dBi at frequencies between 26.5 GHz and 29.5 GHz, and it includes a loss of 3 dB as only half of the test board feed network is utilized in the 4 × 8 array configuration. The simulations are performed using the model of the manufactured 4 × 8 antenna array where each antenna is fed with a wave port directly at the coaxial feed and

FIGURE 16. Measured amplitude and phase of the electric field in front of the antenna array aperture at 28 GHz with the antenna element grid overlaid on top. (a) The amplitude and (b) the phase of the vertical polarization, and (c) the amplitude and (d) the phase of the horizontal polarization.

with a material conductivity of 1.3×10^6 S. The estimations are calculated from the total gain using the simulated losses in the feed network (Fig. 9 and Fig. 11) and the gain of the Anokiwave chips. The first estimation uses the specified gain of 25 dB which results in a gain exceeding the directivity of the simulated antenna array. The second estimation uses a measured chip gain. The gain of the chip was measured using a test board from one port of the chip and it varies between 25 dB and 26.5 dB as a function of frequency. The second estimation results in a more realistic gain approximation for the antenna array not exceeding the directivity. The estimated gain is generally at a lower level than the simulated realized gain. The estimated realized antenna peak gain is 19.8 dB and it is achieved at 28 GHz. Temperature variation during the test and possible gain differences between the chips and antenna ports may result in some errors.

Fig. 19 demonstrates the electrical beam steering of the antenna array with progressive phase shifts when steered from the broadside direction up to ±60° on the vertical plane at 26.5 and 29.5 GHz. The measured beam-steering angle is slightly different at 26.5 and 29.5 GHz as the progressive phase shifts are calculated for 28 GHz resulting in some beam squint. In addition to the broadside direction, the demonstrated beam-steering angles are −60°, −40° −20°, 20°,
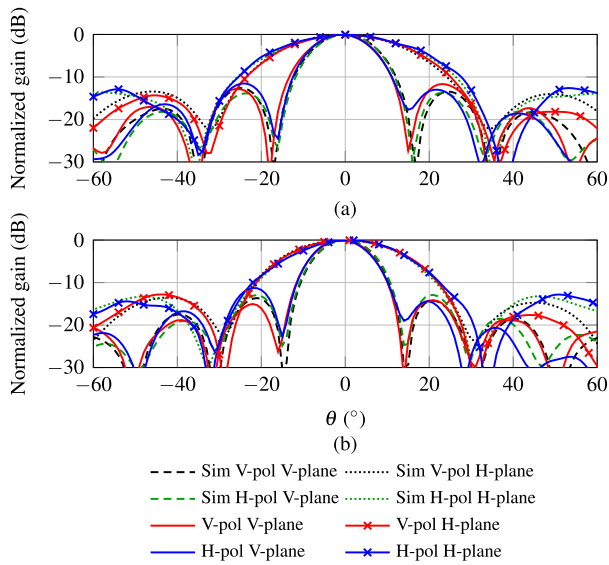
FIGURE 17. Measured and simulated normalized far-field patterns of the V- and H-polarized antenna elements in the vertical and horizontal planes at (a) 26.5 GHz and (b) 29.5 GHz.
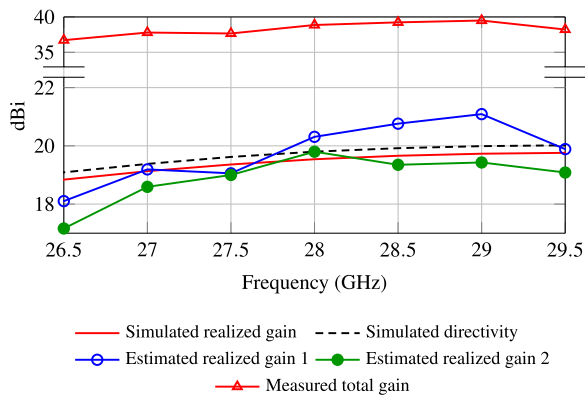

FIGURE 18. Measured and simulated antenna gains. Simulated realized gain and directivity results use an accurate model of the 4 × 8 Vivaldi antenna array. Measured total gain includes the gain of the chips and the losses in the transmission lines. Estimated array gains are calculated from the total gain by removing the gain of the chips and the transmission line losses. First estimation uses the specified 25 dB gain in the chip while the second estimation uses a gain measured using a test board.

FIGURE 19. Measured and simulated normalized far-field patterns at different beam steering angles when steered in the vertical plane. (a) The V-pol patterns at 26.5 GHz, (b) the H-pol patterns at 26.5 GHz, (c) the V-pol patterns at 29.5 GHz and (d) the H-pol patterns at 29.5 GHz.

40°, and 60°. The measured patterns behave extremely well between −40° and 40° being close to identical to the simulated beams. In the case of −60° and 60°, the patterns have a small amount of deviation, and the measured beams taper faster beyond 60° at both frequencies. The faster tapering may be caused by the absorber material used around the antenna aperture to minimize reflections caused by the ground plane where the antenna modules are attached.

Finally, since the RF chips also include gain control, an amplitude weighting along the vertical plane of the antenna array for the vertically polarized elements is demonstrated in Fig. 20. The tapering is arbitrarily selected such that the eight rows on the vertical plane from one to eight are excited with
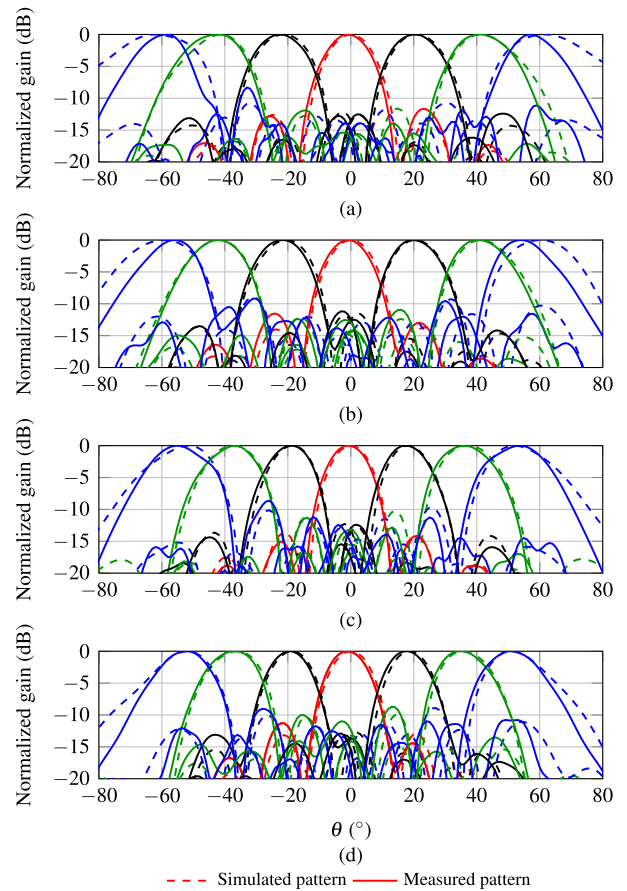
a relative power of −6 dB, −3 dB, −1 dB, 0 dB, 0 dB, −1 dB, −3 dB, −6 dB, respectively. The figure shows that, compared to the uniform excitation, the amplitude tapering decreases the side-lobe level to between −17 to −22 dB whereas the width of the main lobe is increased by 2°. The decrease of the gain cannot be seen from the normalized patterns, but the gain is decreased by 2.2 to 2.4 dB when the tapering is applied.

Table 3 shows a comparison of the proposed modular Vivaldi antenna array structure with the state-of-the-art antenna arrays supporting modularity. The simulated and measured performance of the 30 GHz modular antenna array is in line with the recently published work in the same frequency range. The size of the Vivaldi antenna arrays is larger in height compared to the PCB antennas, and the antenna array or array modules have to be manufactured separately. However, such separate antenna can have some advantages. PCB antennas require additional layers in the PCB. The PCB module in this work uses eight-layer construction while the PCBs in [24] and [25] have 12 layers. The metallic antenna can also be used as a heat sinks when in direct contact with the PCB to conduct heat away from the ICs. Additionally, the Vivaldi antenna structures have a lot wider bandwidth
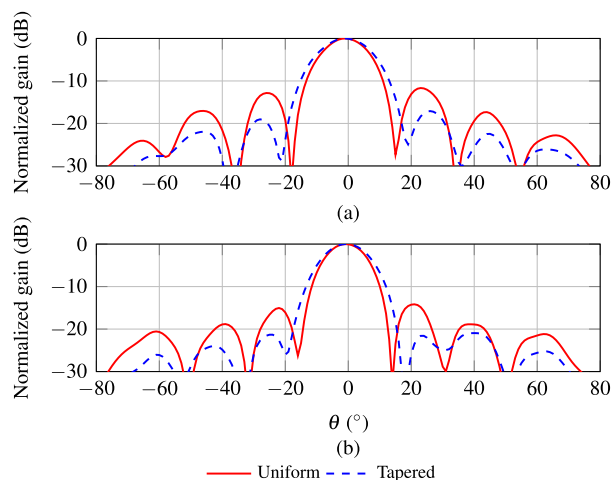
FIGURE 20. Measured far-field patterns of the vertically polarized elements with uniform excitation and with amplitude-tapered excitation at (a) 26.5 GHz and (b) 29.5 GHz.

TABLE 3. Comparison of recent mm-wave antenna arrays at 30 GHz frequency.

	This work	[24]	[25]	[30]
Frequency (GHz)	Antenna: 18–30 ICs: 26.5–29.5[1]	27–31	27.5–31	10–35
Polarization	Dual-Linear	Dual-Linear	Dual-Linear[4]	Single-Linear
Scan range	$\pm 60°$	$\pm 70°$[3]	$\pm 70°$[5]	$\pm 45°$
Antenna type	Metallic (Vivaldi), surface mounted	PCB (patch)	PCB (patch)	Metallic (Vivaldi), separate connectors
Antenna lattice	5 × 5 mm, rectangular	4.67 × 4.67 mm, rectangular	5 × 5 mm, rectangular	4.5 × 4.5 mm, rectangular
Modularity	Yes, 4 × 4 elements	Yes, 32 × 32 elements	Yes, 4 × 4 elements	Yes, 8 × 8[6]
Antenna efficiency, broadside	90-92%[2]	80%	N/A	96%[7]

[1] ICs are interchangeable with a pin compatible 24.25–27.5 GHz model. [2] Antenna metal conductivity = 1.3×10^6 S and including the transmission lines from the ICs to the antennas. [3] $\pm 60°$ with a scan loss of 3 to 3.3 dB. [4] Dual-linear polarized antenna elements connected to a single beam former and RF line. [5] Exact scan loss and antenna performance not indicated. [6] Size of the presented antenna array. [7] Simulation of a fully excited array in the broadside direction.

than the PCB antennas. For example, the antenna array in this work can be configured to operate either at 24.25–27.5 GHz or 26.5–29.5 GHz by simply changing the ICs.

IV. CONCLUSION

A beam-steered dual-polarized modular Vivaldi antenna array design at 30 GHz with integrated electronics is demonstrated. The design includes the antenna module, the RF-module PCB with phase shifters and amplifiers for both polarizations within the antenna module footprint, and the antenna array prototype board that can be used to combine up to four array modules together. The antenna modules are manufactured successfully using additive manufacturing.

The structure is used to demonstrate antenna array operation using two modules in a dual-polarized 4 × 8 antenna element configuration with two separate modules. The combined operation of the modules is demonstrated to be very satisfactory both in simulations as well as measurements.

The measured electric field in front of the antenna array displays consistent amplitude and phase across the whole array aperture. The simulated and measured far-field patterns agree well. The patterns in the V- and H-plane are almost

identical for the both polarizations observed in both the simulations and measurements. The results stay consistent with the simulations also in the beam-steering scenario. Finally, amplitude control is demonstrated successfully by using arbitrary amplitude tapering in the aperture along the vertical plane. The measured total gain of the system is between 35.6 dBi and 39.5 dBi including the 3 dB loss incurred in the power dividers due to only half of the ports being used. The estimated realized antenna gain is close to the simulated realized gain.

The manufactured and measured dual-polarized 30-GHz modular antenna array prototype proves the feasibility of manufacturing high-performance antenna-array elements in small modular parts. The array modules can successfully be used to assemble arrays with various shapes and sizes. The use of identical parts, the antenna and RF modules, decrease the overall cost by decreasing the need to design the antennas and entire RF front ends for all the arrays separately. Additionally, the connectorless interface between the antenna and RF modules decreases cost and the number of components in the assembly even further.

REFERENCES

[1] *Looking Ahead to 5G*, Nokia, Nokia Solutions Netw. Oy, Espoo, Finland, 2013.

[2] J. G. Andrews, S. Buzzi, W. Choi, S. V. Hanly, A. Lozano, A. C. K. Soong, and J. C. Zhang, "What will 5G be?" *IEEE J. Sel. Areas Commun.*, vol. 32, no. 6, pp. 1065–1082, Jun. 2014.

[3] T. S. Rappaport, S. Sun, R. Mayzus, H. Zhao, Y. Azar, K. Wang, G. N. Wong, J. K. Schulz, M. Samimi, and F. Gutierrez, "Millimeter wave mobile communications for 5G cellular: It will work!" *IEEE Access*, vol. 1, pp. 335–349, 2013.

[4] D. Soldani, P. Airas, T. Hoglund, H. Rasanen, and D. Debrecht, "5G to the home," in *Proc. IEEE 85th Veh. Technol. Conf. (VTC Spring)*, Jun. 2017, pp. 1–5.

[5] T. Wild, V. Braun, and H. Viswanathan, "Joint design of communication and sensing for beyond 5G and 6G systems," *IEEE Access*, vol. 9, pp. 30845–30857, 2021.

[6] R. W. Kindt and J. T. Logan, "Benchmarking ultrawideband phased antenna arrays: Striving for clearer and more informative reporting practices," *IEEE Antennas Propag. Mag.*, vol. 60, no. 3, pp. 34–47, Jun. 2018.

[7] H. Holter, T.-H. Chio, and D. H. Schaubert, "Experimental results of 144-element dual-polarized endfire tapered-slot phased arrays," *IEEE Trans. Antennas Propag.*, vol. 48, no. 11, pp. 1707–1718, Nov. 2000.

[8] H. Holter, "Dual-polarized broadband array antenna with BOR-elements, mechanical design and measurements," *IEEE Trans. Antennas Propag.*, vol. 55, no. 2, pp. 305–312, Feb. 2007.

[9] D. H. Schaubert, S. Kasturi, A. O. Boryssenko, and W. M. Elsallal, "Vivaldi antenna arrays for wide bandwidth and electronic scanning," in *Proc. 2nd Eur. Conf. Antennas Propag. (EuCAP)*. Edison, NJ, USA: IET, Nov. 2007, pp. 1–6.

[10] J. T. Logan, R. W. Kindt, and M. N. Vouvakis, "A 1.2–12 GHz sliced notch antenna array," *IEEE Trans. Antennas Propag.*, vol. 66, no. 4, pp. 1818–1826, Apr. 2018.

[11] S. Livingston and J. J. Lee, "A low profile wide band dual-pol array with coincident phase center for next generation radars," in *Proc. IET Int. Conf. Radar Syst. (Radar)*. Edison, NJ, USA: IET, Oct. 2012, pp. 1–5.

[12] J. Massman, G. Simpson, and T. Steffen, "Low cost additively manufactured antenna array modules," in *Proc. IEEE Int. Symp. Phased Array Syst. Technol. (PAST)*, Oct. 2019, pp. 1–4.

[13] S. S. Holland and M. N. Vouvakis, "The planar ultrawideband modular antenna (PUMA) array," *IEEE Trans. Antennas Propag.*, vol. 60, no. 1, pp. 130–140, Jan. 2012.

[14] S. S. Holland, D. H. Schaubert, and M. N. Vouvakis, "A 7–21 GHz dual-polarized planar ultrawideband modular antenna (PUMA) array," *IEEE Trans. Antennas Propag.*, vol. 60, no. 10, pp. 4589–4600, Oct. 2012.

[15] J. T. Logan and M. N. Vouvakis, "Planar ultrawideband modular antenna (PUMA) arrays scalable to mm-waves," in *Proc. IEEE Antennas Propag. Soc. Int. Symp. (APSURSI)*, Jul. 2013, pp. 624–625.

[16] R. Kindt, R. Mital, and M. Vouvakis, "3:1-bandwidth millimeter-wave Puma array," in *Proc. IEEE Int. Symp. Antennas Propag. (APSURSI)*, Jun. 2016, pp. 1867–1868.

[17] J. R. LaCroix and M. N. Vouvakis, "Low-cost PUMA array on a BGA package," in *Proc. IEEE Int. Symp. Antennas Propag. North Amer. Radio Sci. Meeting*, Jul. 2020, pp. 1629–1630.

[18] Z. Siddiqui, M. Sonkki, K. Rasilainen, J. Chen, M. Berg, M. E. Leinonen, and A. Pärssinen, "Dual-polarized filtering antenna for mm-wave 5G base station antenna array," in *Proc. 15th Eur. Conf. Antennas Propag. (EuCAP)*, Mar. 2021, pp. 1–4.

[19] Z. Siddiqui, M. Sonkki, J. Chen, M. Berg, M. E. Leinonen, and A. Pärssinen, "Dual-band dual-polarized antenna for mm-wave 5G base station antenna array," in *Proc. 14th Eur. Conf. Antennas Propag. (EuCAP)*, Mar. 2020, pp. 1–4.

[20] D. Zhao, P. Gu, J. Zhong, N. Peng, M. Yang, Y. Yi, J. Zhang, P. He, Y. Chai, Z. Chen, and X. You, "Millimeter-wave integrated phased arrays," *IEEE Trans. Circuits Syst. I, Reg. Papers*, vol. 68, no. 10, pp. 3977–3990, Oct. 2021.

[21] G. Gultepe, S. Zihir, T. Kanar, and G. M. Rebeiz, "A dual-polarized 1024-element Ku-band SATCOM transmit phased-array with ±70° scan and 43.5 dBW EIRP," in *IEEE MTT-S Int. Microw. Symp. Dig.*, Aug. 2020, pp. 837–840.

[22] K. Kibaroglu, M. Sayginer, and G. M. Rebeiz, "A low-cost scalable 32-element 28-GHz phased array transceiver for 5G communication links based on a 2 × 2 beamformer flip-chip unit cell," *IEEE J. Solid-State Circuits*, vol. 53, no. 5, pp. 1260–1274, May 2018.

[23] L. Wang, J. Geng, K. Wang, H. Zhou, C. Ren, H. Wu, X. Zhao, C. He, X. Liang, W. Zhu, and R. Jin, "Wideband dual-polarized binary coding antenna with wide beamwidth and its array for millimeter-wave applications," *IEEE Antennas Wireless Propag. Lett.*, vol. 19, no. 4, pp. 636–640, Apr. 2020.

[24] K. K. W. Low, S. Zihir, T. Kanar, and G. M. Rebeiz, "A 27–31-GHz 1024-element Ka-band SATCOM phased-array transmitter with 49.5-dBW peak EIRP, 1-dB AR, and ±70° beam scanning," *IEEE Trans. Microw. Theory Techn.*, vol. 70, no. 3, pp. 1757–1768, Mar. 2022.

[25] W. M. Abdel-Wahab, H. Al-Saedi, E. H. M. Alian, M. Raeis-Zadeh, A. Ehsandar, A. Palizban, N. Ghafarian, G. Chen, H. Gharaee, M. R. Nezhad-Ahmadi, and S. Safavi Naeini, "A modular architecture for wide scan angle phased array antenna for *K*/Ka mobile SATCOM," in *IEEE MTT-S Int. Microw. Symp. Dig.*, Jun. 2019, pp. 1076–1079.

[26] J.-C.-S. Chieh, E. Yeo, R. Farkouh, A. Castro, M. Kerber, R. B. Olsen, E. J. Merulla, and S. K. Sharma, "Development of flat panel active phased array antennas using 5G silicon RFICs at Ku- and Ka-bands," *IEEE Access*, vol. 8, pp. 192669–192681, 2020.

[27] H. Kähkönen, J. Ala-Laurinaho, and V. Viikari, "Surface-mounted Ka-band Vivaldi antenna array," *IEEE Open J. Antennas Propag.*, vol. 2, pp. 126–137, 2021.

[28] H. Kahkonen, J. A.-Laurinaho, and V. Viikari, "Dual-polarized Ka-band Vivaldi antenna array," *IEEE Trans. Antennas Propag.*, vol. 68, pp. 2675–2683, 2020.

[29] H. Kähkönen, S. Proper, J. Ala-Laurinaho, and V. Viikari, "Comparison of additively manufactured and machined antenna array performance at Ka-band," *IEEE Antennas Wireless Propag. Lett.*, vol. 21, no. 1, pp. 9–13, Jan. 2022.

[30] M. A. Elmansouri, G. R. Friedrichs, L. B. Boskovic, and D. S. Filipovic, "An X-band through Ka-band thinned all-metal Vivaldi phased array," *IEEE Trans. Antennas Propag.*, vol. 69, no. 11, pp. 7613–7623, Nov. 2021.

HENRI KÄHKÖNEN was born in Lohja, Finland, in 1989. He received the B.Sc. (Tech.) and M.Sc. (Tech.) degrees in electrical engineering from Aalto University, Espoo, Finland, in 2015 and 2017, respectively. He is currently pursuing the joint D.Sc. (Tech.) degree with Saab AB and the Department of Electronics and Nanoengineering, School of Electrical Engineering, Aalto University. He has been a Research Assistant with Aalto University, since 2016. His current research interests include wideband, beam steerable antenna arrays, and especially at millimeter wave spectrum.

JUHA ALA-LAURINAHO received the Diploma Engineering (M.Sc.) degree in mathematics and the D.Sc. (Tech.) degree in electrical engineering from the Helsinki University of Technology (TKK), Finland, in 1995 and 2001, respectively. He has been with TKK (currently Aalto University), working with the Radio Laboratory, from 1995 to 2007, the Department of Radio Science and Engineering, from 2008 to 2016, and currently with the Department of Electronics and Nanoengineering. In 1995, he worked as a Research Assistant and, since 1996, he has been a Research Associate and currently, he is working as a Staff Scientist. He has been a Researcher and a Project Manager in many millimeter-wave technology related projects. His current research interests include the antennas and antenna measurement techniques for millimeter and submillimeter waves and the millimeter wave imaging.

VILLE VIIKARI (Senior Member, IEEE) received the Master of Science (Tech.) and Doctor of Science (Tech.) (Hons.) degrees in electrical engineering from the Helsinki University of Technology (TKK), Espoo, Finland, in 2004 and 2007, respectively.

He is currently a Professor and the Deputy Head of the Department with the School of Electrical Engineering, Aalto University, Espoo. From 2001 to 2007, he was with the Radio Laboratory, TKK (now part of Aalto University), where he studied antenna measurement techniques at submillimeter wavelengths and antenna pattern correction techniques. From 2007 to 2012, he was a Research Scientist and a Senior Scientist with the VTT Technical Research Centre, Espoo, where his research included wireless sensors, RFID, radar applications, MEMS, and microwave sensors. He was appointed as an Assistant Professor with Aalto University, in 2012. He has authored or coauthored about 85 journal articles and 90 conference papers. He is an inventor in 16 granted patents. His current research interests include antennas for mobile devices and networks, antenna clusters and coupled arrays, RF-powered devices, and antenna measurement techniques.

Dr. Viikari is a Regional Delegate of EurAAP. He was a recipient of the Young Researcher Award of the Year 2014, presented by the Finnish Foundation for Technology Promotion and IEEE Sensors Council 2010 Early Career Gold Award.

● ● ●